eNeuro

Research Article: New Research

Disorders of the Nervous System

Visual System Hyperexcitability and Compromised V1 Receptive Field Properties in Early-Stage Retinitis Pigmentosa in Mice

Henri Leinonen,[1,2] David C. Lyon,[3] Krzysztof Palczewski,[2] and Andrzej T. Foik[4]

https://doi.org/10.1523/ENEURO.0107-22.2022

[1]School of Pharmacy, Faculty of Health Sciences, University of Eastern Finland, 70211 Kuopio, Finland, [2]Gavin Herbert Eye Institute, Department of Ophthalmology, University of California, Irvine, CA 92697, [3]Department of Anatomy & Neurobiology, University of California, Irvine, CA 92697, and [4]Ophthalmic Biology Group, International Centre for Translational Eye Research, Institute of Physical Chemistry, Polish Academy of Sciences, 01-224 Warsaw, Poland

Abstract

Inherited retinal degenerative diseases are a prominent cause of blindness. Although mutations causing death of photoreceptors are mostly known, the pathophysiology downstream in the inner retina and along the visual pathway is incompletely characterized in the earliest disease stages. Here, we investigated retinal, midbrain and cortical visual function using electroretinography (ERG), the optomotor response (OMR), visual evoked potentials (VEPs), respectively, and single unit electrophysiology at the primary visual cortex (V1) in light-adapted juvenile (approximately one-month-old) and young adult (three-month-old) *Rho*$^{P23H/WT}$ mice, representative of early-stage retinitis pigmentosa (RP). Photopic ERG revealed up to ~30% hypersensitivity to light in *Rho*$^{P23H/WT}$ mice, as measured by the light intensity required to generate half-maximal b-wave (I_{50} parameter). *Rho*$^{P23H/WT}$ mice also showed increased OMRs toward low spatial frequency (SF) drifting gratings, indicative of visual overexcitation at the midbrain level. At the V1 level, VEPs and single-cell recordings revealed prominent hyperexcitability in the juvenile *Rho*$^{P23H/WT}$ mice. Mean VEP amplitudes for light ON stimuli were nearly doubled in one-month-old *Rho*$^{P23H/WT}$ mice compared with controls, and more than doubled for light OFF. Single-cell recordings showed a significantly increased spontaneous V1 neuron firing in the *Rho*$^{P23H/WT}$ mice, and persistent contrast and temporal sensitivities. In contrast, direction selectivity was severely compromised. Our data suggest that during early RP, the visual pathway becomes hyperexcited. This could have both compensatory and deleterious consequences for visual behavior. Further studies on the mechanisms of hyperexcitability are warranted as this could lead to therapeutic interventions for RP.

Key words: blindness; photoreceptors; primary visual cortex; retina; retinal degeneration; visual processing

Significance Statement

Lost retinal function in many blinding retinal degenerative disorders could soon be alleviated by advanced therapies that restore photoreception. However, it is unknown whether a visual system rewired downstream of the photoreceptors can process signals adequately. We studied the functional consequences of early rod death along the visual pathway in young retinitis pigmentosa (RP) mice. Photopic inner retina responses were moderately hypersensitized in the electroretinograms (ERG) of RP mice. Reflex-based visual behavior and visual cortex electrophysiology showed hyperexcitability. Some aspects of complex visual processing were remarkably resistant to degeneration, whereas others were severely impacted. We conclude that the visual system adapts to lost photoreception by increasing sensitivity, but simultaneously becomes detrimentally hyperexcited. Mechanistic understanding could lead to therapeutic preservation and restoration of vision.

Introduction

Consequences of total or near total loss of outer retinal photoreceptors, rods and cones, to the inner retina function have been widely studied using animal models of retinal degenerative diseases (D'Orazi et al., 2014; Strettoi, 2015; Pfeiffer et al., 2020; Strettoi et al., 2022). With respect to clinical correlates, corresponding anatomic data have been obtained from patient retinas postmortem (Jones et al., 2016). Such studies have demonstrated robust rewiring of neural connections, commonly referred to as "remodeling," leading to dramatically increased spontaneous neural activity, decreased signal-to-noise ratios, and attenuated light responses in the inner retina (Toychiev et al., 2013; Trenholm and Awatramani, 2015; Haselier et al., 2017; Telias et al., 2020). Much concern has been raised that retinal remodeling may preclude restoration of visual function even if augmentation of photoreception by various advanced therapies could be achieved (Marc et al., 2014; Reh, 2016; Foik et al., 2018; Suh et al., 2020). By default, this refractoriness would be particularly problematic in the adult organism with limited capability for neural plasticity and presumed inability to adapt to and properly process the restored sensory signals.

Much less attention has been directed to investigating functional outcomes of early retinal degeneration and milder disease stages, although most patients with retinal degeneration suffer from a partial loss of vision, and some may never become legally blind (Berson et al., 2002; Xu et al., 2020). Studies focusing on early disease stages could help us understand the triggers and mechanisms of retinal remodeling and lead to increased ability to develop vision restoration interventions. Equally important, increased mechanistic understanding could help us design therapies to increase quality of life in patients with partial loss of vision because of retinal degeneration.

Most inherited retinal degenerations are classified under the umbrella term retinitis pigmentosa (RP). In a typical RP case, primarily rod photoreceptors are affected first; consequently the disease first manifests as loss of night vision and shrinking of the visual field (Hartong et al., 2006). Central and color vision impairment manifest only at a much more advanced disease state. RP phenotype has been studied extensively with respect to the primary insult, rod degeneration and dysfunction. Investigation of the cone-associated phenotype has gained somewhat less attention, although the secondary cone degeneration may be a more realistic target for conventional pharmacological interventions. In fact, preservation of cone-pathway function could retain the most important attributes of vision for humans, such as color vision and high visual acuity. Another gap in knowledge exists in how visual signals are modulated in the brain during early RP. This is crucial as the complex circuitry in the inner retina, which ultimately sends the visual signals to the rest of the brain, rewires early in RP (Soto and Kerschensteiner, 2015). In the current study, we addressed these issues by using an established animal model of autosomal dominant RP (heterozygote $Rho^{P23H/WT}$ mice) before cone degeneration, and by recording photopic electroretinography (ERG), behavioral optomotor responses (OMRs), and primary visual cortex (V1) responses to light ON-OFF and multimodal pattern stimuli.

Materials and Methods

Animals

A mouse model of autosomal dominant RP was used in this study. The mouse carries a P23H mutation in the rhodopsin gene, causing a phenotype of extremely fast rod photoreceptor degeneration in homozygous mutants ($Rho^{P23H/P23H}$), and an intermediately fast progressing rod degeneration in heterozygous mutants ($Rho^{P23H/WT}$; Sakami et al., 2011, 2014). This report mainly focuses on the heterozygous mutants. As is common for the RP phenotype (Hartong et al., 2006), cone photoreceptor degeneration is much delayed in $Rho^{P23H/WT}$ mice (Sakami et al., 2011, 2014). The $Rho^{P23H/WT}$ mice were generated by crossbreeding $Rho^{P23H/P23H}$ mice with wild-type (WT) C57BL/6J mice (The Jackson Laboratory, stock # 000664). Age-matched WT mice were used as controls. Both male and female mice were used that were group-housed in a standard vivarium using *ad libitum* feeding. The light-dark cycle was set at 12 h/12 h (lights on 6:30 A.M., lights off 6:30 P.M.). Cone-transducin knock-out mice ($Gnat2^{-/-}$, a kind gift of Marie Burns, UC Davis), that lack cone-mediated function but do not show retinal degeneration (Ronning et al., 2018), were used for calibration of photopic ERG background (Extended Data Fig. 1-1). In all procedures, animal subjects were treated following the NIH guidelines for the care and use of laboratory animals,

Received March 14, 2022; accepted June 3, 2022; First published June 14, 2022.

K.P. is Chief Scientific Officer of Polgenix Inc. All authors declare no competing financial interests.

Author contributions: H.L., D.C.L., K.P., and A.T.F. designed research; H.L. and A.T.F. performed research; D.C.L., K.P., and A.T.F. contributed unpublished reagents/analytic tools; H.L. and A.T.F. analyzed data; H.L., D.C.L., K.P., and A.T.F. wrote the paper.

This work was supported by the National Institute of Health Grant R01EY009339 (to K.P.) and the National Institutes of Health Grant R24EY027283 (to K.P.). H.L. was supported by the Academy of Finland Grant 346295, by a Knights Templar Eye Foundation Career Starter Grant, and by grants from the Finnish Cultural Foundation, the Orion Research Foundation, the Eye and Tissue Bank Foundation (Finland), Retina Registered Association (Finland), and Sokeain Ystävät/De Blindas Vänner Registered Association. This work was also supported by the National Science Center, Poland Grant 2019/34/E/NZ5/00434 (to A.T.F.); The International Centre for Translational Eye Research (MAB/2019/12) project is carried out within the International Research Agendas programme of the Foundation for Polish Science co-financed by the European Union under the European Regional Development Fund (A.T.F.).

Acknowledgments: We thank Dr. Vladimir Kefalov for valuable comments during manuscript preparation. We also thank our colleagues at University of California, Irvine Center for Translational Vision Research and Gavin Herbert Eye Institute for helpful comments regarding this study. Dr. Palczewski is the Donald Bren Professor and the Irving H. Leopold Chair of Ophthalmology.

Correspondence should be addressed to Henri Leinonen at henri.leinonen@uef.fi or Andrzej T. Foik at afoik@ichf.edu.pl.

https://doi.org/10.1523/ENEURO.0107-22.2022

Table 1: Conversion of luminous energy to radiance units

cd·s/m^2	0.03	0.05	0.1	0.3	0.5	1	3	10	30	100
UV, mW/sr/m^2	1.53	2.55	5.09	15.27	25.46	50.92	152.75	509.16	n.a.	n.a.
Green, mW/sr/m^2	n.a.	n.a.	n.a.	0.64	1.07	2.14	6.41	21.35	64.06	213.52

Conversion coefficients are as follows: 0.002135 W/sr/m^2 = 1 photopic cd·s/m^2 for the green light; and 0.050915 W/sr/m^2 = 1 photopic cd·s/m^2 for the UV light. Note, the Diagnosys Espion ERG software uses luminance units by default.

and the ARVO Statement for the Use of Animals in Ophthalmic and Vision Research; and under a protocol approved by the Institutional Animal Care and Use Committee of UC Irvine (AUP-18-124).

ERG

The ERG was performed under standard laboratory lighting conditions using a Diagnosys Celeris rodent ERG device (Diagnosys), with some modifications from a previous protocol (Orban et al., 2018). The mice were anesthetized with ketamine (100 mg/kg, KetaVed; Bioniche Teoranta, Inverin Co) and xylazine (10 mg/mg, Rompun; Bayer) by intraperitoneal injection, and their pupils were dilated with 1% tropicamide (Tropicamide Ophthalmic Solution USP 1%; Akorn), and thereafter kept moist with 0.3% hypromellose gel (GenTeal; Alcon). Light stimulation was produced by an in-house scripted simulation series in Espion software (version 6; Diagnosys). The eyes were stimulated with a green light-emitting diode (LED; peak 544 nm, bandwidth 160 nm) or with a UV LED (peak emission 370 nm, bandwidth 50 nm). While green stimulation was used, the steady rod-suppressing background light consisted of 200 cd/m^2 red (peak 630 nm, bandwidth 100 nm) and 100 cd/m^2 UV. The background during UV stimulation consisted of 200 cd/m^2 red and 100 cd/m^2 green. Steady red light at 200 cd/m^2 suppresses the ERG signal practically fully in *Gnat2*$^{-/-}$ mice (Extended Data Fig. 1-1). However, a steady strong UV or green background at 100 cd/m^2 was further added to facilitate rod suppression during monochromatic green or UV flash stimulation, respectively. Seven different green light stimulus intensities between 0.64 and 214 mW/sr/m^2, and eight different UV intensities between 1.53 and 509 mW/sr/m^2, were used in ascending order. The whole stimulation protocol lasted <10 min. Stimulus intensities in radiance units were obtained from measurements and conversion coefficients provided by Diagnosys LLC. The details of conversion of luminous energy units to radiance units are presented in Table 1.

The ERG signal was acquired at 2 kHz and filtered with a low-frequency cutoff at 0.25 Hz and a high-frequency cutoff at 300 Hz. Espion software automatically detected the ERG a-wave (first negative ERG component) and b-wave (first positive ERG component) amplitudes; a-wave amplitude was measured from the signal baseline, whereas b-wave amplitude was measured as the difference between the negative trough (a-wave) and the highest positive peak. For assessment of retinal light sensitivity ($I_{1/2}$), b-wave amplitudes were fitted as a function of stimulus intensity by using the Naka–Rushton equation (Naka and Rushton, 1966), wherein the $I_{1/2}$ parameter describes the light intensity needed to exert half-maximal b-wave.

OMR behavioral vision test

The OMRs were assessed using a commercial OMR platform (Phenosys qOMR, PhenoSys GmbH) that utilizes automated head tracking and behavior analysis, following protocols described elsewhere (Suh et al., 2020). The OMR arena was lit at ~80 lux, corresponding to the photopic light level. Rotating (12° s^{-1}) vertical sinusoidal grating stimuli at various spatial frequencies (SFs) were presented for 11 min per trial to light-adapted mice. The contrast between the white and black gratings was set at 100%, whereas the SF (0.05, 0.1, 0.15, 0.20, 0.25, 0.30, 0.35, 0.375, 0.40, 0.425, 0.45 cycles per degree of visual angle; CPD) pattern changed every 60 s in a random order, with one exception; each session always started with 0.1 CPD to facilitate acclimatization to the task, as this SF is known to evoke reliable OMR in WT mice. Each mouse was tested in at least four trials. The performances across the trials were averaged for analysis, excluding those 60-s stimulus periods that led to a correct/incorrect ratio smaller than 0.8. All experiments were performed in the morning before noon.

Single-unit and local field potential (LFP) recordings and visual stimulation

Mice were initially anesthetized with 2% isoflurane in a mixture of N_2O/O_2 (70%/30%), then placed into a stereotaxic apparatus. A small, custom-made plastic chamber was glued (Vetbond) to the exposed skull. After 1 d of recovery, re-anesthetized animals were placed in a custom-made hammock, maintained under isoflurane anesthesia (1–2% in N_2O/O_2), and multiple single tungsten electrodes were inserted into a small craniotomy above the visual cortex. Once the electrodes were inserted, the chamber was filled with sterile agar and sealed with sterile bone wax. During recording sessions, animals were sedated with chlorprothixene hydrochloride (1 mg/kg, i.m.; Camillo et al., 2018) and kept under light isoflurane anesthesia (0.2–0.4% in 30% O_2). EEG and EKG were monitored throughout the experiments, and body temperature was maintained with a heating pad (Harvard Apparatus).

Data were acquired using a 32-channel Scout recording system (Ripple). The LFP from multiple locations was bandpass filtered from 0.1 to 250 Hz and stored together with spiking data on a computer with a 1-kHz sampling rate. The LFP signal was cut according to stimulus time stamps and averaged across trials for each recording location to calculate visually evoked potentials (VEPs; Foik et al., 2015; Kordecka et al., 2020; Suh et al., 2020; Lewandowski et al., 2022). The spike signal was bandpass filtered from 500 Hz to 7 kHz and stored in a computer hard drive at a 30-kHz sampling frequency. Spikes

were sorted online in Trellis (Ripple) while performing visual stimulation. Visual stimuli were generated in MATLAB (MathWorks) using Psychophysics Toolbox (Brainard, 1997; Pelli, 1997; Kleiner et al., 2007) and displayed on a γ-corrected LCD monitor (55 inches, 60 Hz; 1920 × 1080 pixels; 52 cd/m^2 mean luminance). Stimulus onset times were corrected for LCD monitor delay using a photodiode and microcontroller (in-house design; Foik et al., 2018).

The vision quality was assessed using protocols published in our previous work (Foik et al., 2018, 2020; Kordecka et al., 2020; Suh et al., 2020). For recordings of visually evoked responses, cells were first tested with 100 repetitions of a 500-ms bright flash of light (105 cd/m^2). Receptive fields for visually responsive cells were then located using square-wave drifting gratings, after which optimal orientation/direction, SF and temporal frequency (TF) were determined using sine-wave gratings. SFs tested were from 0.001 to 0.5 cycles/°. TFs tested were from 0.1 to 10 cycles/s. With these optimal parameters, size tuning was assessed using apertures of 1–110° at 100% contrast. With the optimal size, temporal and SF, and at high contrast, the orientation tuning of the cell was tested again using eight orientations × two directions each, stepped by 22.5° increments. This was followed by testing contrast. Single units were recorded along the whole depth of the primary visual cortex (V1) as presented in previous studies (Foik et al., 2018; Suh et al., 2020; Frankowski et al., 2021; Choi et al., 2022; Lewandowski et al., 2022).

VEP data analysis

The response amplitude of LFP was calculated as a difference between the peak of the positive and negative components in the VEP wave. The response latency was defined as the time point where maximum response occurred. The maximum of the response was defined as the maximum of either the negative or positive peak.

Tuning curves were calculated based on the average spike rate. Optimal visual parameters were chosen as the maximum response value. Orientation tuning was measured in degrees as the half-width at half-height (HWHH; 1.18 × σ) based on fits to Gaussian distributions (Carandini and Ferster, 2000; Alitto and Usrey, 2004; Foik et al., 2018, 2020) using:

$$R_{O_s} = baseline + R_p e^{\frac{-(O_s - O_p)^2}{2\sigma^2}} + R_n e^{\frac{-(O_s - O_p + 180)^2}{2\sigma^2}},$$

where O_s is the stimulus orientation, R_{Os} is the response to different orientations, O_p is the preferred orientation, R_p and R_n are the responses at the preferred and non-preferred direction, σ is the tuning width, and "baseline" is the offset of the Gaussian distribution. Gaussian fits were estimated without subtracting spontaneous activity, similar to the procedures of Alitto and Usrey (Alitto and Usrey, 2004).

Size tuning curves were fitted by a difference of Gaussian (DoG) function:

$$R_s = K_e \int_{-s}^{s} e^{\left(\frac{-x}{r_e}\right)^2} dx - K_i \int_{-s}^{s} e^{\left(\frac{-x}{r_i}\right)^2} dx + R_0,$$

in which R_s is the response evoked by different aperture sizes. The free parameters, K_e and r_e, describe the strength and the size of the excitatory space, respectively; K_i and r_i represent the strength and the size of the inhibitory space, respectively; and R_0 is the spontaneous activity of the cell.

The optimal SF and TF were extracted from the data fitted to Gaussian distributions using the following equation (DeAngelis et al., 1993; Van Den Bergh et al., 2010; Foik et al., 2018, 2020):

$$R_{\frac{SF}{TF}} = baseline + R_{pref} e^{\frac{-\left(\frac{SF}{TF} - \frac{SF}{TFpref}\right)^2}{2\sigma^2}},$$

where $R_{SF/TF}$ is the estimated response, R_{pref} indicates response at a preferred SF or TF. SF/TF indicates SF or TF, σ is the SD of the Gaussian, and the baseline is the Gaussian offset.

The contrast tuning was fitted by using the Naka–Rushton equation (Naka and Rushton, 1966; Albrecht and Hamilton, 1982; Van Den Bergh et al., 2010; Przybyszewski et al., 2014; Foik et al., 2018):

$$R(C) = \frac{gC^n}{C_{50}^n + C^n},$$

where g is the gain (response), contrast at the 50% of the maximum response (C_{50}) is the contrast at mid response, and n is the exponent. For the contrast tuning fit the background activity was subtracted from the response curve, and values below background SD were changed to 0, as done elsewhere (Van Den Bergh et al., 2010; Foik et al., 2018).

Spectral dissection of ERG and VEP responses

The ERG and VEPs were filtered using fourth order Butterworth bandpass filters of 13–29 Hz for β, and 30–120 Hz for γ ranges. Two filtered signals for each animal were then used to calculate amplitude spectra using the fast Fourier transform (FFT) algorithm (MATLAB) and amplitude spectrum area (AMSA), and shown as bar plots. The dominant frequencies in β and γ ranges were picked for each animal separately as the frequency at maximum amplitude in the calculated spectrum. This process was repeated for each animal in each group and for green and UV light intensities to create the frequency versus light intensity and AMSA versus light intensity traces.

Statistical analysis

Data throughout the manuscript are presented as mean ± SEM. The level of statistical significance was set at $p < 0.05$. The ERG light intensity series were analyzed by two-way repeated measures ANOVA (RM ANOVA), using the light intensity as the within-subjects factor (repeated) and genotype as the between-subjects factor. Sidak's *post hoc*

tests were applied if ANOVA found a significant between-subjects main effect, or within between-subjects interaction. Retinal light sensitivity ($I_{1/2}$) was analyzed by Welch's *t* test. In the OMR data, the genotypes were compared using regular two-way ANOVA, whereas repeated measurements in the same animals (e.g., WT animals at one vs three months of age) were analyzed using two-way RM ANOVA by age as the repeated factor. GraphPad Prism 9 software was used for ERG and OMR data analysis. Data from cortical recordings and oscillatory activity was analyzed with the Kruskal–Wallis test followed by Dunn–Sidak *post hoc* tests. Cortical recording and oscillatory activity offline data analysis and statistics were performed in MATLAB (MathWorks).

Results

Increased photopic ERG b-wave sensitivity in *Rho*$^{P23H/WT}$ mice

We began our investigations by recording photopic ERGs in light-adapted one-month-old mice (Fig. 1*A–H*). Because mouse S- and M-cones are most sensitive for UV and green light, with peak sensitivities at around 360 and 510 nm (Jacobs et al., 1991; Lyubarsky et al., 1999), respectively, and since S- and M-cones could be differentially affected during retinal degeneration (Greenstein et al., 1989; Schwarz et al., 2018; Hassall et al., 2020), we recorded photopic ERGs using both monochromatic UV light and green light stimuli. The a-wave or b-wave response amplitudes did not show an overall difference between genotypes as determined by RM ANOVA (a-wave, Extended Data Fig. 1-2*A*,*B*; b-wave, Fig. 1*B*,*F*). However, anecdotally *Rho*$^{P23H/WT}$ mice seemed to display higher amplitudes at intermediate light intensities (Fig. 1*B*,*F*). Therefore, we used the Naka–Rushton function for curve fitting (Naka and Rushton, 1966) and derivatization of light intensity required to generate half-maximal b-wave responses ($I_{1/2}$) as a measure of retinal light sensitivity. We found decreased $I_{1/2}$, indicative of increased sensitivity, in *Rho*$^{P23H/WT}$ mice for both green light (Fig. 1*C*) and UV light (Fig. 1*G*) stimulation, which supports previous findings (Leinonen et al., 2020). In addition, b-wave peak latency on average was faster in *Rho*$^{P23H/WT}$ mice as compared with WT mice (Fig. 1*A*,*H*), but this trend toward shorter latency did not reach a statistically significant value (green, $p = 0.09$; UV, $p = 0.20$). Instead, the a-wave latency was significantly faster in response to a UV flash in one-month-old *Rho*$^{P23H/WT}$ mice compared with WT (Extended Data Fig. 1-2*F*), but not in response to a green flash (Extended Data Fig. 1-2*E*, $p = 0.73$).

To study whether increased photopic ERG sensitivity is persistent in adulthood, we performed the same recordings at three months of age (Fig. 1*I–P*). Here, the maximal b-wave amplitudes in *Rho*$^{P23H/WT}$ mice tended to remain slightly lower compared with WT (Fig. 1*J*,*N*), although no significant RM ANOVA effects were found for the amplitude comparisons (green, $p = 0.25$; UV, $p = 0.76$). Instead, RM ANOVA revealed a significant light intensity-response amplitude interaction both in response to green light (Fig. 1*J*, $p < 0.05$) and UV light (Fig. 1*N*, $p < 0.001$) stimulation. The RM ANOVA interaction together with visual inspection of light intensity-response amplitude curves (Fig. 1*J*, *N*) indicate that although maximal b-wave amplitudes tended to decrease in *Rho*$^{P23H/WT}$ mice, responses to intermediate light intensities were above WT level. Indeed, *Rho*$^{P23H/WT}$ mice still showed significantly decreased $I_{1/2}$ b-wave sensitivity parameters compared with WT mice (Fig. 1*K*,*O*), regardless of intermediate retinal degeneration at this stage (Sakami et al., 2011; Leinonen et al., 2020). We interpret the relative decrease in b-amplitude and increase in b-wave latency in *Rho*$^{P23H/WT}$ mice between one and three months of age (compare Fig. 1*B*, *D*,*F*,*H* and *J*,*L*,*N*,*P*) to reflect a disease stage when cone degeneration is commencing, although there were not yet decreases in a-wave amplitudes at this age range (Extended Data Fig. 1-2). Overall, the modest photopic ERG changes which we observed in *Rho*$^{P23H/WT}$ mice appeared to be more evident in the S-cone pathway as compared with the M-cone pathway.

To provide a context for how the advanced-disease stage represents a cone-mediated retinal function, we recorded photopic ERGs also in one-month-old homozygous mutant (*Rho*$^{P23H/P23H}$) mice with an almost complete loss of photoreceptors by this age (Sakami et al., 2011). These recordings demonstrated only a residual response in the cone-pathway (Fig. 1*A*,*B*,*E*,*F*; Extended Data Fig. 1-3), which rendered curve fitting, light sensitivity, and response latency assessments impractical.

Prominent oscillatory potentials (OPs) ride on the ascending phase of the rodent ERG b-wave and could have implications on the b-wave analyses. We therefore performed OP amplitude and peak frequency analyses at two distinct ranges: β (13–29 Hz) and γ (30–120 Hz; Extended Data Fig. 1-4). The OP amplitude was significantly attenuated in Rho$^{P23H/P23H}$ mice as expected, because of extreme retinal degeneration and resulting minimal input from photoreceptors. Instead, there were no significant differences between the *Rho*$^{P23H/WT}$ and WT mice either in amplitude spectrum area (AMSA) or dominant frequency parameter at any of the conditions, except for one: *Rho*$^{P23H/WT}$ mice displayed a higher dominant frequency than WT mice in response to the strongest UV flash at the β range (Extended Data Fig. 1-4). Overall, OPs cannot explain the increased b-wave sensitivity observed in *Rho*$^{P23H/WT}$ mice (Fig. 1).

Rho$^{P23H/WT}$ mice display increased optomotor movements toward low SF drifting patterns

We next sought to determine whether visual acuity, an elementary visual behavior as measured by OMRs, is changed in light-adapted/photopic conditions in 1.5- and 3-month-old *Rho*$^{P23H/WT}$ mice. An earlier report using OMR found contrast sensitivity was well-preserved in *Rho*$^{P23H/WT}$ mice even in scotopic conditions despite prominent rod death (Leinonen et al., 2020). Here, we used a commercial OMR setup coupled with an automated head-tracking system (Kretschmer et al., 2013, 2015), which allowed us to record the mouse optomotor movements with respect to the drifting pattern in its visual field at 30 frames per second. The common OMR studies

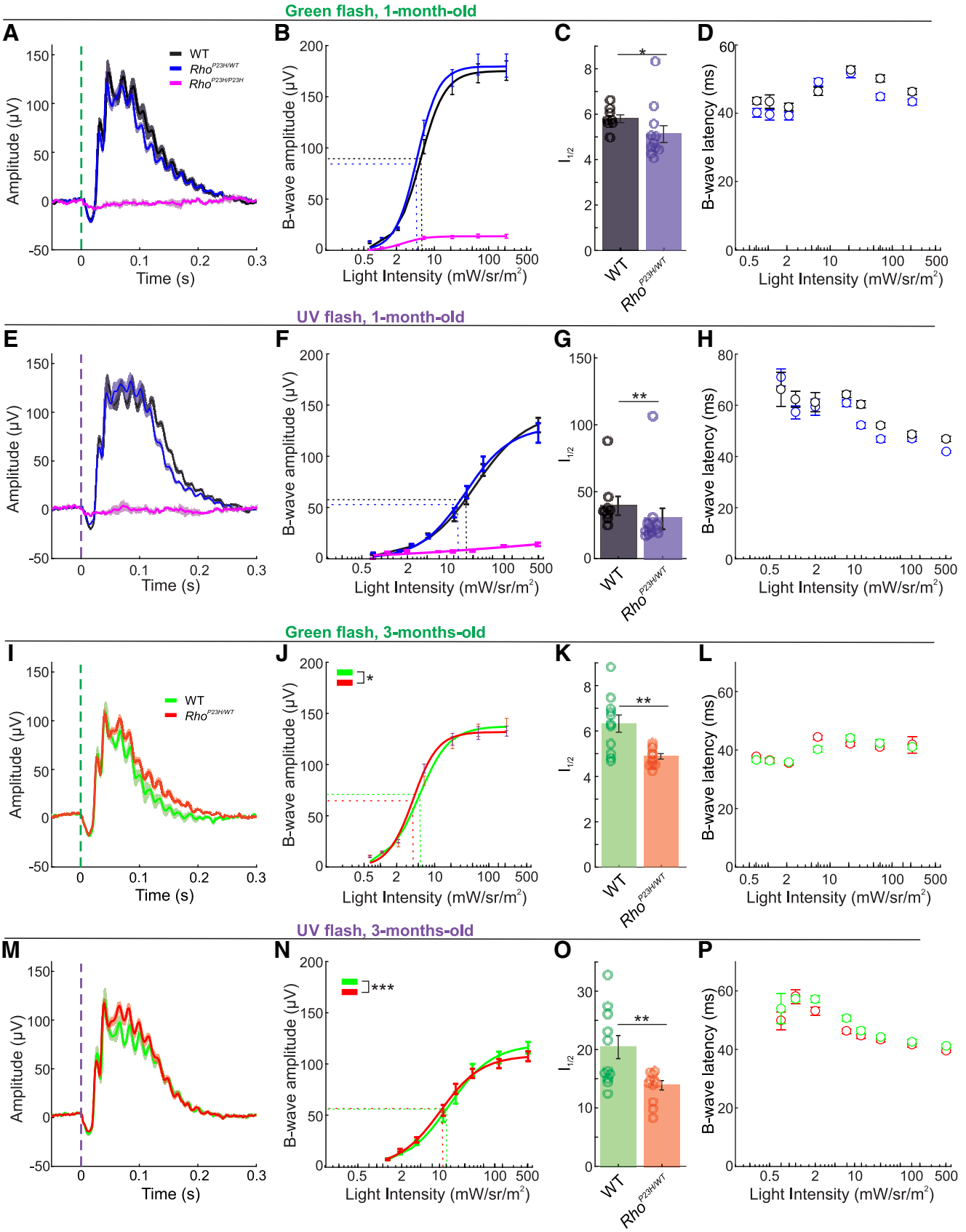

Figure 1. Increased light sensitivity in cone-dominant ERGs in *Rho*$^{P23H/WT}$ mice. Panels ***A–H*** present data from one-month-old mice, and panels I-P correspond to three-month-old mice. Extended Data Figure 1-1 presents background light calibration for the

continued

photopic ERG. ***A***, ERG waveforms in response to a 214 mW·sr/m^2 green light flash (peak emission 544 nm, bandwidth 160 nm; black/gray lines, WT, $n = 8$; blue, *Rho*$^{P23H/WT}$, $n = 11$; magenta, *Rho*$^{P23H/P23H}$, $n = 4$). Lines represent group averages ± SEM. Extended Data Figure 1-2 presents ERG waveforms in all conditions. Extended Data Figure 1-3 shows spectrally dissected oscillatory potentials from ERG waveforms. ***B***, b-Wave amplitude series and (***C***) b-wave sensitivity ($I_{1/2}$) to green light flash. ***D***, b-Wave latency series to green flash. ***E***, ERG waveforms in response to a 509 mW·sr/m^2 UV flash (peak emission 370 nm, bandwidth 50 nm). ***F***, b-Wave amplitude series. ***G***, b-Wave sensitivity ($I_{1/2}$) to UV light flash. ***H***, b-Wave latency series. ***I***, ERG waveforms in response to a 214 mW·sr/m^2 green flash in three-month-old mice (green lines, WT, $n = 11$; red, *Rho*$^{P23H/WT}$, $n = 11$). ***J***, b-Wave amplitude series (light intensity-response amplitude interaction, $p < 0.05$). ***K***, $I_{1/2}$ for green light flash. ***L***, b-Wave latency series for green flash. ***M***, ERG waveforms in response to 509 mW·s/m^2 UV flash in three-month-old mice. ***N***, b-Wave amplitude series for UV flashes (light intensity-response amplitude interaction, $p < 0.001$). ***O***, $I_{1/2}$ for UV light flash. ***P***, b-Wave latency series for UV flash. RM two-way ANOVA were applied to amplitude and latency analyses in the increasing flash intensity series. $I_{1/2}$ was acquired from curve fitting, following the Naka–Rushton equation and derivation of light intensity required to generate a half-maximal response. Comparisons for the $I_{1/2}$ parameter were performed by Welch's *t* test. Data are presented as mean ± SEM, plus individual replicates (circles) in ***C***, ***G***, ***K***, ***O***. $^*p < 0.05$, $^{**}p < 0.01$, $^{***}p < 0.001$.

have typically investigated the SF (visual acuity assessment) or contrast threshold detection limits using subjective assessment. In contrast, our paradigm ranks correct/incorrect optomotor movements at every frame, providing a more sensitive and objective means to document "supernormal" visual behavior. At the highest SF (smallest pattern sizes) the stimuli elicited similar responses in the 1.5-month-old *Rho*$^{P23H/WT}$ mice and WT mice; however, with the *Rho*$^{P23H/WT}$ mice, optomotor movements toward stimuli at the lowest SF (largest pattern size) were more frequent than those of WT mice, as demonstrated by their higher OMR index (Fig. 2*A*). This behavior reflects sensorimotor hypersensitivity to low SF drifting patterns in the visual field of the *Rho*$^{P23H/WT}$ mice. The same mice performed the same task later at three months of age. Head-tracking behavior in *Rho*$^{P23H/WT}$ mice slightly decreased between 1.5 and 3 months of age (Fig. 2*B*), indicating an initial decline in visual acuity in three-month-old *Rho*$^{P23H/WT}$ mice. Still, *Rho*$^{P23H/WT}$ mice at three months of age continued with a supernormal OMR at low SF, as compared with same-age WT mice (Fig. 2*C*; OMR index-SF interaction, $p < 0.05$). Intact responses in WT mice between 1.5 and 3 months of age document the feasibility of the repeated analysis (Fig. 2*D*, $p = 0.49$).

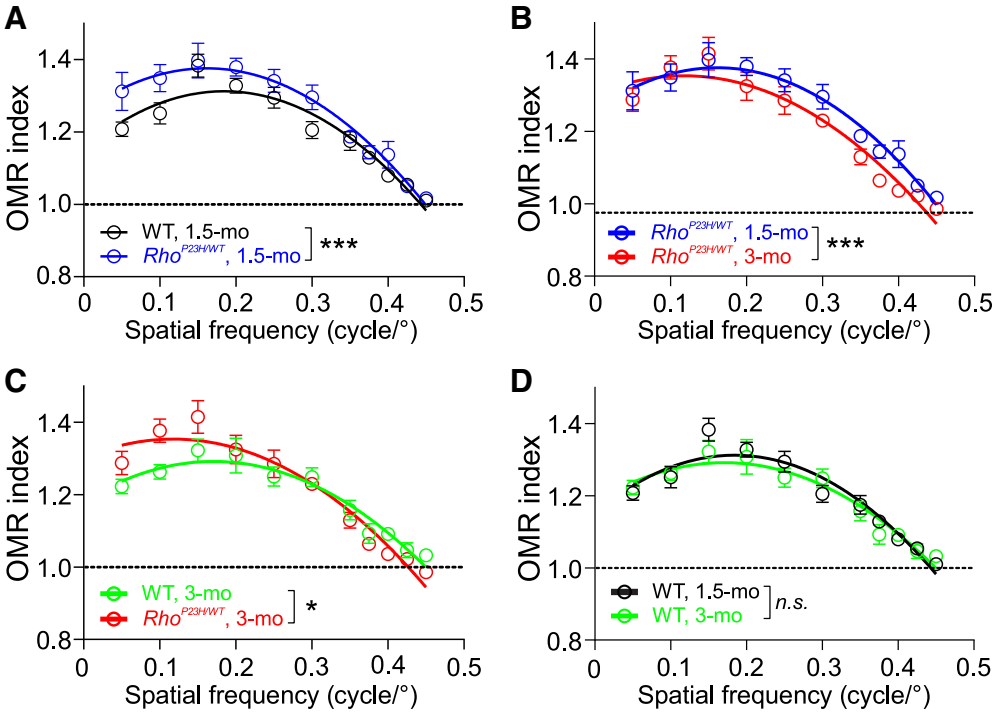

Figure 2. Hypersensitized OMR to low SF drifting gratings in *Rho*$^{P23H/WT}$ mice. ***A***, Group comparison of WT ($n = 8$) and *Rho*$^{P23H/WT}$ ($n = 10$) mice at 1.5 months of age (genotype effect: $^{***}p < 0.001$). ***B***, Repeated analysis in *Rho*$^{P23H/WT}$ mice at 1.5 and 3 months of age (age effect: $^{***}p < 0.001$). ***C***, Group comparison of WT ($n = 8$) and *Rho*$^{P23H/WT}$ ($n = 10$) mice at three months of age (OMR index-SF interaction: $^*p < 0.05$). ***D***, Repeated analysis in WT mice at 1.5 and 3 months of age (age effect: $p = 0.49$). The statistical analysis was performed using two-way RM ANOVA. OMR index-SF interaction in ***C*** signifies opposing sensitivity differences between WT and *Rho*$^{P23H/WT}$ groups at low versus high SF. n.s., nonsignificant. Data are presented as mean ± SEM. Lines that represent second-order quadratic polynomial fits are for illustration and were not used in the analysis.

Stimulus-dependent and spontaneous visual cortex hyperexcitability in juvenile *Rho*$^{P23H/WT}$ mice

Most importantly for central vision, it was important to investigate the consequences of early retinal degeneration for light responses at the V1 level (note, OMR is a subcortically originating reflex and does not require V1 function; Douglas et al., 2005). To this end, we started by recording VEPs in response to light ON/light OFF stimuli. We found an increase in both ON and OFF responses in one-month-old *Rho*$^{P23H/WT}$ mice compared with same-age WT mice (Fig. 3*A–C*,*E*), indicating hyperexcitability. Conversely, the same age homozygous *Rho*$^{P23H/P23H}$ mutants showed only a residual response as expected, because of severe retinal degeneration and dysfunction (Fig. 3*C*,*E*; Sakami et al., 2011). Heterozygous *Rho*$^{P23H/WT}$ mice at three months old, when more than half of their photoreceptors are gone (Leinonen et al., 2020), still showed VEP amplitude comparable to WT mice (Fig. 3*C*, *E*). The response latency to the ON stimulus increased with disease severity (Fig. 3*D*, $p < 0.01$), whereas latency to the OFF stimulus remained intact in heterozygous mutants (Fig. 3*F*).

To investigate whether oscillatory activity is also affected in V1 in response to ON and OFF stimuli, we analyzed AMSA as well as dominant oscillation frequency at β (13–29 Hz), and γ frequency (30–120 Hz) ranges (Fig. 4*A*,*B* and *E*,*F*, respectively). As with the main VEP component amplitudes, we found on average higher AMSAs in the β (Fig. 4*B*,*C*) and γ (Fig. 4*F*,*G*) frequency ranges in one-month-old *Rho*$^{P23H/WT}$ mice, although far from statistical significance ($p = 0.33$ and $p = 0.46$, respectively). Instead, by three months of age, the amplitude of oscillatory activity lowered substantially in *Rho*$^{P23H/WT}$ mice and reached levels similar to WT (Fig. 4*B*,*C*; $p = 0.79$). As expected, AMSAs at both β and γ ranges were significantly lower in the most advanced disease stage studied, in *Rho*$^{P23H/P23H}$ mice (Fig. 4*B*,*C*,*F*,*G*). We found no differences in dominant oscillation ranges at either the β (Fig. 4*D*, $p = 0.13$) or γ (Fig. 4*H*, $p = 0.3$) ranges. Overall, the lack of major differences in dominant oscillatory frequencies suggests no change in large network processing in the brain.

Single-unit recordings corroborated significant visual cortex hyperexcitability in the juvenile *Rho*$^{P23H/WT}$ mice (Fig. 5). Both light ON and light OFF conversions evoked more spiking activity in one-month-old *Rho*$^{P23H/WT}$ mice relative to WT (Fig. 5*A*,*B*,*G*,*H*). One should note, however, that more than half of the V1 neurons in *Rho*$^{P23H/WT}$ mice did not respond to the light stimulus, whereas in WT mice $<10\%$ of units were nonresponsive (Fig. 5*E*). The cortical hyperexcitability in juvenile *Rho*$^{P23H/WT}$ mice was not only stimulus-dependent but also continuous as the stimulus-independent background spiking was also significantly elevated in the juvenile *Rho*$^{P23H/WT}$ mice versus WT (Fig. 5*A*,*B*,*F*). The spiking activity diminished in the mutant mice with disease progression, so that average spiking activity to light ON or OFF did not differ between three-month-old *Rho*$^{P23H/WT}$ and WT mice (Fig. 5*A*,*C*,*G*,*H*). Notably, however, light ON responses in *Rho*$^{P23H/WT}$ mutants were qualitatively abnormal regardless of age, as highlighted by the second peak in spiking activity occurring at ~200 ms or later from light onset (Fig. 6*C*), a phenomenon that was absent in the WT mice (Fig. 5*A*). The spiking pattern at light OFF remained relatively normal in *Rho*$^{P23H/WT}$ mutants (Fig. 5*A–C*). As expected, the spiking activity to both light ON or light OFF was significantly dampened in the homozygous *Rho*$^{P23H/P23H}$ mice (Fig. 5*D*,*G*,*H*). Conversely, the spontaneous spiking activity was *increased* in late-stage disease (*Rho*$^{P23H/P23H}$) compared with the less advanced disease stage (three-month-old *Rho*$^{P23H/WT}$; Fig. 5*F*), indicating that some phenomenon independent of photoreceptors begins to drive spontaneous V1 neuron spiking in late-stage retinal degeneration, similar to what has been proposed previously regarding activity recordings of cone bipolar, amacrine, and retinal ganglion cells (RGCs; Borowska et al., 2011; Menzler and Zeck, 2011).

Compromised tuning properties of V1 neurons to drifting pattern stimuli

We last investigated V1 neuron tuning properties in *Rho*$^{P23H/WT}$ mice. For this task, we used drifting sinusoidal-pattern stimuli to study several different parameters relevant for visual behavior: orientation/direction tuning, SF tuning, as well as thresholds for SF, contrast, and TF. Several abnormalities were observed in *Rho*$^{P23H/WT}$ mice. First, the orientation tuning curve was distinctly broader compared with WT mice already at one month of age (Fig. 6*A*,*B*). Strikingly, the three-month-old *Rho*$^{P23H/WT}$ mice practically preferred no directions, demonstrating a dramatic loss of directional selectivity. Next, the pattern size to which mice optimally responded increased with disease progression, indicating enlargement of receptive fields (Fig. 6*C*,*D*). The optimal SF was slightly decreased at one month old for *Rho*$^{P23H/WT}$ mice, and severely decreased by the age of three months (Fig. 6*E*,*F*). In contrast, the optimal TF was abnormally high in one-month-old *Rho*$^{P23H/WT}$ mice (Fig. 6*G*,*H*), mirroring hastened kinetics of retinal responses to light stimulation (Fig. 1*D*,*H*; Extended Data Fig. 1-2*F*). Also, the contrast sensitivity in *Rho*$^{P23H/WT}$ mice remained at similar levels to those for WT mice, even at three months of age (Fig. 6*I*,*J*). Altogether, the VEP and V1 single-unit recordings observed in young *Rho*$^{P23H/WT}$ mice reveal that hastened ERG kinetics (Fig. 1*D*,*H*; Extended Data Fig. 1-2*F*; Pasquale et al., 2021), maintained behavioral contrast and TF thresholds (Leinonen et al., 2020; Pasquale et al., 2021), and increased preference for lower SF stimuli (Fig. 2*A*,*C*) are reflected in V1 function. We were unable to record meaningful responses to pattern stimuli in the most advanced disease state, in *Rho*$^{P23H/P23H}$ mice.

Discussion

Consequences of early rod degeneration to photopic visual function

Previous studies have suggested paradoxical sensitization of cone-mediated retinal function in the earliest stages of rod degeneration in mice (Leinonen et al., 2017, 2020). To investigate this phenomenon further, we recorded photopic ERG responses in *Rho*$^{P23H/WT}$ mice at

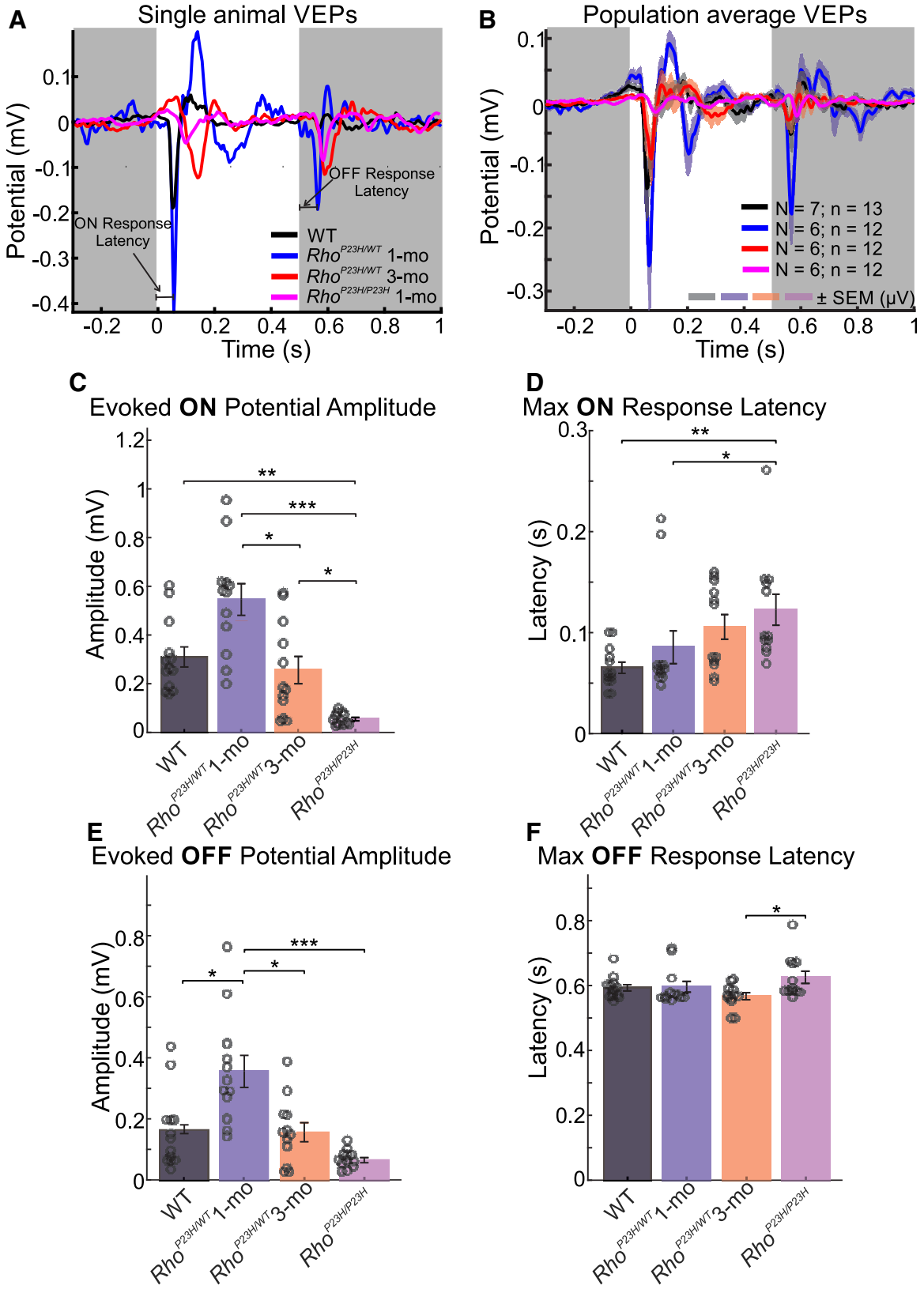

Figure 3. Supernormal VEPs for light ON/light OFF stimuli in juvenile *Rho*$^{P23H/WT}$ mice. White and gray backgrounds in ***A***, ***B*** indicate the period when the light was ON or OFF, respectively. ***A***, Representative VEP waveforms from a single WT mouse (black), a one-month-old *Rho*$^{P23H/WT}$ mouse (blue line), a three-month-old *Rho*$^{P23H/WT}$ mouse (red), and a one-month-old *Rho*$^{P23H/P23H}$ mouse (magenta). Horizontal lines indicate ON-response latency or OFF-response latency, as indicated. ***B***, Group-averaged VEP waveforms

continued
(WT, $N = 7$ mice, $n = 13$ eyes; one-month-old *Rho*$^{P23H/WT}$, $N = 6$ mice, $n = 12$ eyes; three-month-old *Rho*$^{P23H/WT}$, $N = 6$ mice, $n = 12$ eyes; one-month-old *Rho*$^{P23H/P23H}$, $N = 6$ mice, $n = 12$ eyes). The colored shading in ***B*** indicates ± SEM from the response mean. ***C***, ON response amplitudes. ***D***, ON response latencies. ***E***, OFF response amplitudes. ***F***, OFF response latencies. Data are presented as mean ± SEM, plus individual replicates (circles) in ***C–F***. The statistical analysis was performed using the Kruskal–Wallis test followed by Dunn–Sidak *post hoc* tests: $^{*}p < 0.05$, $^{**}p < 0.01$, $^{***}p < 0.001$.

one and three months of age, when ~20% and ~60% of rods have degenerated, respectively; but cone count remains normal (Leinonen et al., 2020). Maximal photopic ERG responses were intact in one-month-old *Rho*$^{P23H/WT}$ mice, indicating a lack of cone degeneration at this age (Fig. 1; Extended Data Fig. 1-2). Instead, the sensitivity of the b-wave was enhanced compared with WT controls. At three months of age, the increase in b-wave sensitivity became even more apparent in *Rho*$^{P23H/WT}$ mice despite their maximal b-wave amplitude showing some trend toward a decline (Fig. 1). In a more advanced stage of RP, the cone function undoubtedly declines (Sakami et al., 2011; Leinonen et al., 2020). Increased b-wave sensitivity in rod-specific function in *Rho*$^{P23H/WT}$/*Gnat2*$^{-/-}$ mice have been recently observed, regardless of prominent rod degeneration (Leinonen et al., 2020). Relatively better-preserved ERG b-waves as compared with a-waves have been reported also in P23H transgenic rats (Machida et al., 2000; Aleman et al., 2001). The reason for increased sensitivity of the ERG b-wave is unknown but may include overcompensation of the gain at the photoreceptor-to-bipolar synapse in response to outer retina degeneration.

The kinetics of photopic ERG b-wave responses showed a trend (not statistically significant) toward hastening in one-month-old *Rho*$^{P23H/WT}$ mice (Fig. 1). The a-wave response was significantly hastened in *Rho*$^{P23H/WT}$ mice in response to UV stimulation (Extended Data Fig. 1-2). Pasquale et al., recently reported significantly improved temporal contrast sensitivity (TCS) in *Rho*$^{P23H/WT}$ mice (Pasquale et al., 2021). The improvement arose from the rod-pathway, as the phenomenon remained when *Rho*$^{P23H/WT}$ mice were crossed with GNAT2$^{cpfl3/cpfl3}$ mice that lack cone function. This could be explained by faster photo-response kinetics

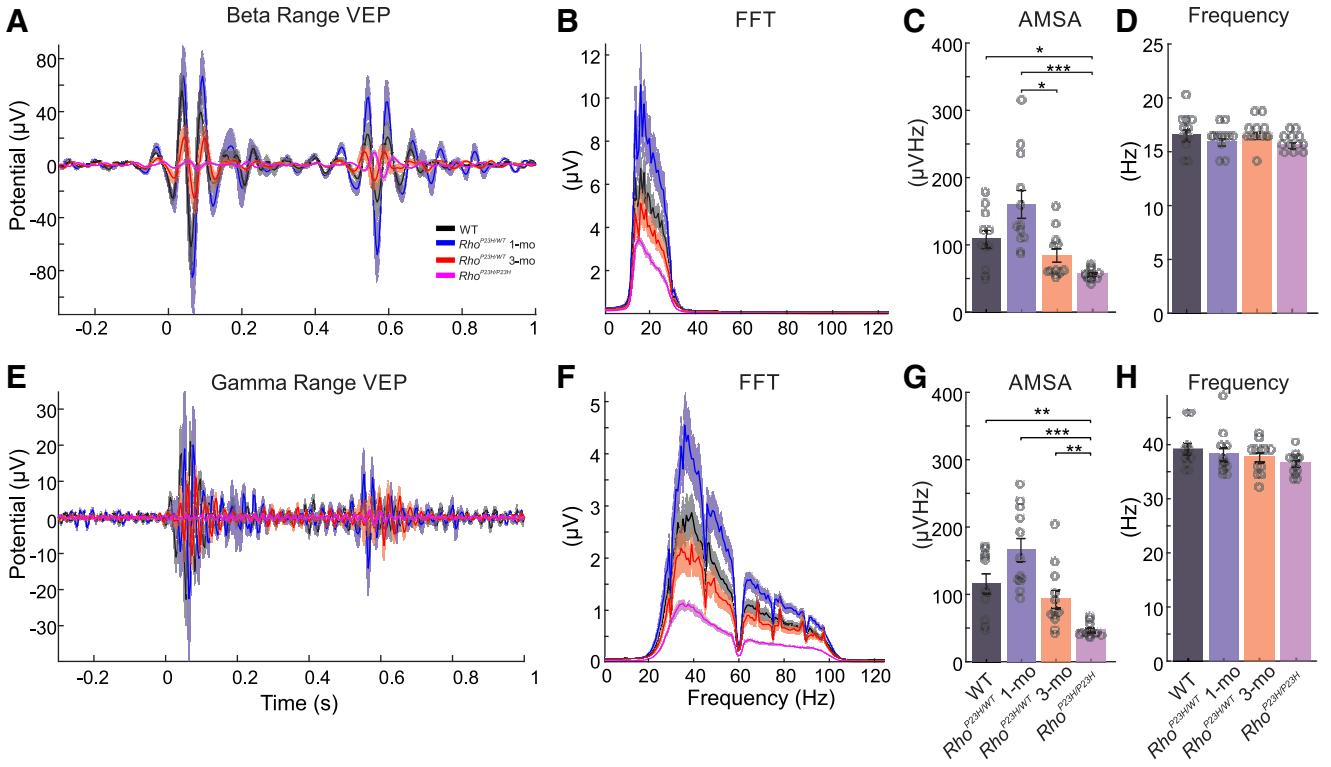

Figure 4. Increased oscillatory activity in response to light in V1 of juvenile *Rho*$^{P23H/WT}$ mice. β And γ range oscillations in VEP responses to light flash are shown similarly to analyses presented in Extended Data Figure 1-4. ***A***, Average cortical VEPs for all animal groups were filtered using the bandpass filter in the β frequency range (13–29 Hz). ***B***, Corresponding FFT spectra are shown. ***C***, Comparison of population-average AMSAs on the β frequency range. ***D***, Comparison of population-average dominant oscillation frequencies in the beta frequency range. ***E***, Average cortical VEPs for all groups were filtered using the bandpass filter in the γ range (30–120 Hz). ***F***, Amplitude spectra were calculated for each animal group. ***G***, Comparison of AMSA values among all groups in the γ frequency range. ***H***, Population-average dominant frequencies of oscillations in the γ range. Circles indicate individual recording sites. The Kruskal–Wallis test was performed, followed by Dunn–Sidak *post hoc* tests: $^{*}p < 0.05$, $^{**}p < 0.01$, $^{***}p < 0.001$.

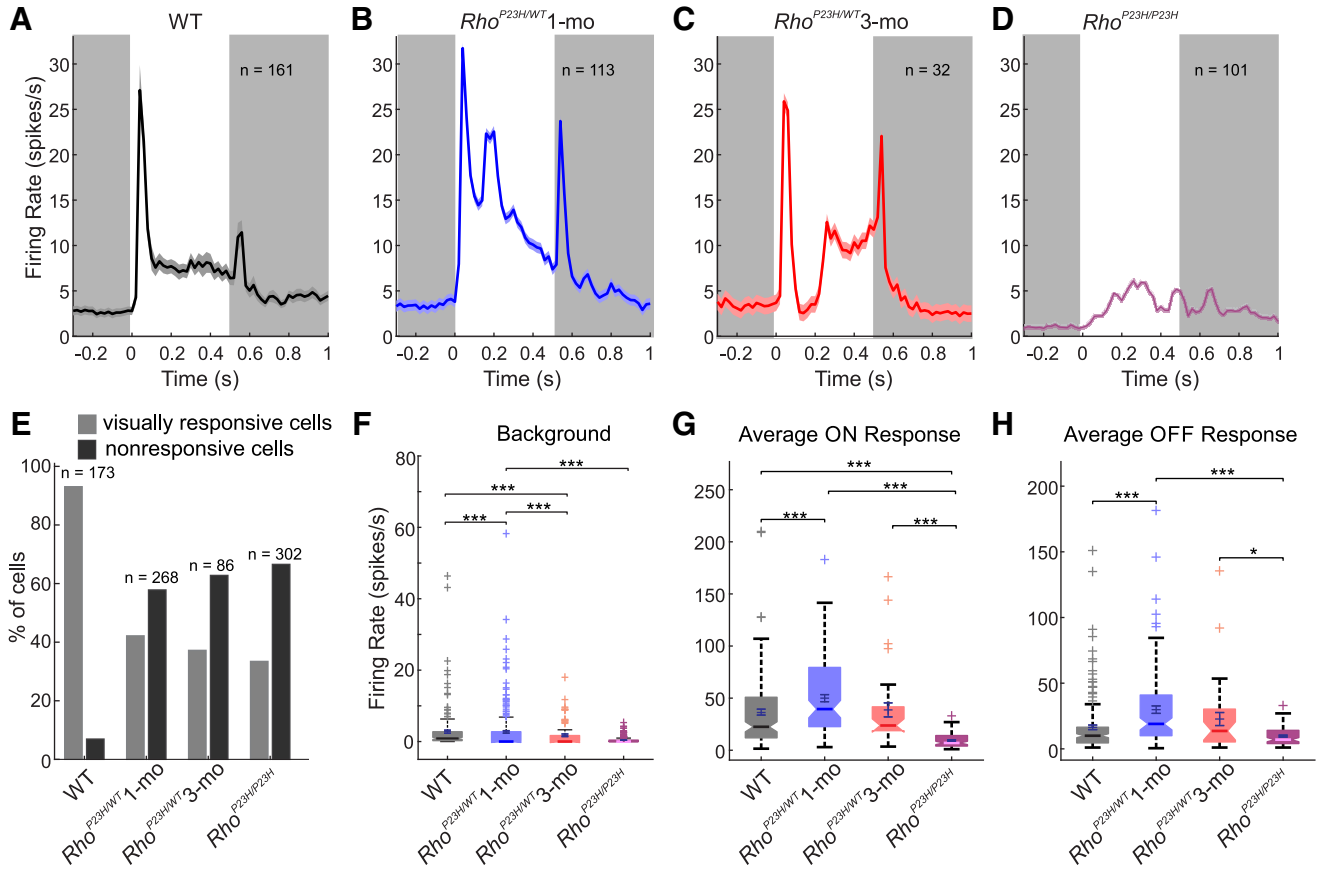

Figure 5. Cortical neurons are hyperexcited in juvenile *Rho*$^{P23H/WT}$ mice. White and gray backgrounds in ***A***, ***B*** indicate the period when the light was ON or OFF, respectively. ***A***, Population summary of single-neuron responses to light ON/OFF stimuli for WT mice ($N = 7$ mice, $n = 161$ neurons); (***B***) one-month-old *Rho*$^{P23H/WT}$ mice ($N = 6$ mice, $n = 113$ neurons); (***C***) three-month-old *Rho*$^{P23H/WT}$ mice ($N = 6$ mice, $n = 32$ neurons); and (***D***) one-month-old *Rho*$^{P23H/P23H}$ mice ($N = 6$ mice, $n = 101$ neurons). ***E***, Percentage of visually responsive and nonresponsive neurons in each group. ***F***, Background firing rate without light stimulus. ***G***, Maximum firing rate at light ON for each group. ***H***, Maximum firing rate at light OFF for each group. Each box plot (***F–H***) indicates a median marked by a solid line and a notch. The bottom and top edges of the boxes indicate 25th and 75th percentiles, and whiskers indicate maximum and minimum values in distributions. Crosses indicate individual values treated as outliers. Kruskal–Wallis test followed by Dunn–Sidak *post hoc* tests: $^{*}p < 0.05$, $^{**}p < 0.01$, $^{***}p < 0.001$.

and decreased density and collecting area of rods in *Rho*$^{P23H/WT}$ mice (Sakami et al., 2014; Pasquale et al., 2021). The mechanism that explains faster initial rod response is unclear, but could be related to volume changes in the rod outer segment or changes in Ca^{2+} dynamics (Pasquale et al., 2021). Our recent transcriptomic profiling of *Rho*$^{P23H/WT}$ retina homogenates supports the latter, as we showed significant pathway enrichments in, e.g., calmodulin binding and ion-channel-activity-related genes, including cation channel activities (Leinonen et al., 2020). However, analysis at single-cell resolution is needed to test whether these changes occur in the rods or elsewhere in the retina.

As no clear deterioration of photopic ERG was observed in *Rho*$^{P23H/WT}$ mice up to three months of age, and since scotopic contrast sensitivity is remarkably resistant to early rod degeneration (Leinonen et al., 2020), we were curious to see whether any visual acuity change by OMR measures would occur at this disease stage. To this end, we used an OMR system coupled with automated head-tracking (Kretschmer et al., 2015). During the 60 s recording period per SF, the system recorded 1800 frames, and at every frame compared optomotor movements to correct and incorrect directions, rendering an optomotor index. Since the OMR is a reflex-based visual task, we hypothesized that increased tracking toward the drifting patterns (or increased OMR index) by light-adapted *Rho*$^{P23H/WT}$ mice was possible. This was partially true, as the OMR index at low SF for the *Rho*$^{P23H/WT}$ mouse was higher compared with that for the WT mouse (Fig. 2). At high SF, the OMR index was equal between genotypes at 1.5 months, indicating intact visual acuity in *Rho*$^{P23H/WT}$ mice. However, between 1.5 and 3 months of age, the OMR index at high SF slightly declined in *Rho*$^{P23H/WT}$ mice, indicating an initial decrease in visual acuity by three months in *Rho*$^{P23H/WT}$ mice. With respect to rod-driven night vision, a strong link between enhanced scotopic ERG b-wave sensitivity and well-maintained OMR in *Rho*$^{P23H/WT}$ and *Rho*$^{P23H/WT}$/*Gnat2*$^{-/-}$ mice was recently demonstrated (Leinonen et al., 2020).

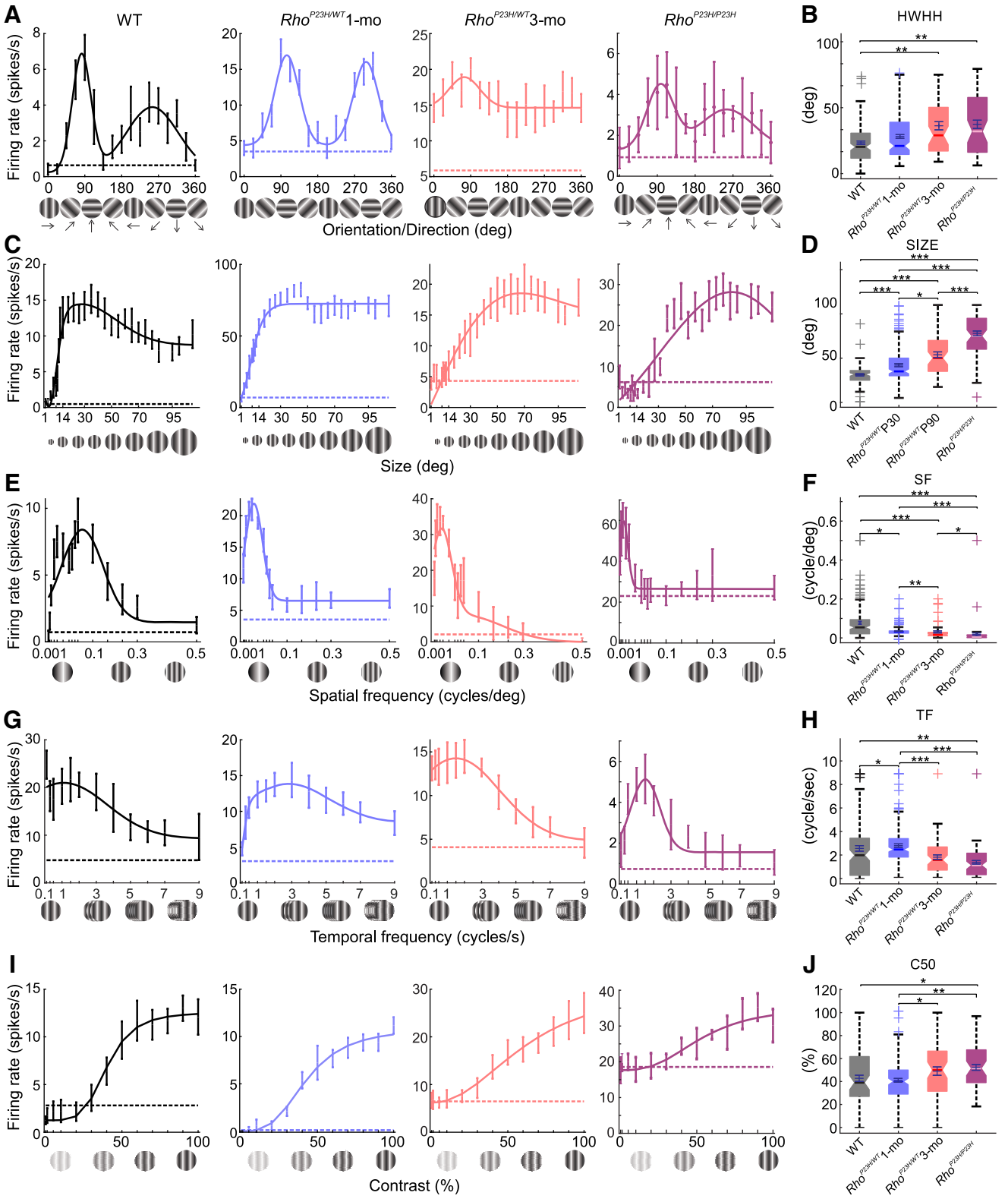

Figure 6. Altered V1 neuron-tuning properties in *Rho*$^{P23H/WT}$ mice. ***A***, Representative orientation/direction tuning curves of single cells for all groups. ***B***, Orientation tuning is measured as HWHH (WT, black, $N = 7$ mice, $n = 153$ neurons; one-month-old *Rho*$^{P23H/WT}$, blue, $N = 6$ mice, $n = 189$ neurons; three-month-old *Rho*$^{P23H/WT}$, blue, $N = 6$ mice, $n = 116$ neurons; one-month-old *Rho*$^{P23H/P23H}$, magenta, $N = 6$ mice, $n = 88$ neurons). ***C***, Representative stimulus size tuning curves of single cells. ***D***, Stimulus size at which maximal firing rate was observed. ***E***, Representative SF tuning curves of single cells. ***F***, SF at which maximal firing rate was observed. ***G***, Representative TF tuning curves of single cells. ***H***, Drifting pattern speed at which maximal firing rate was observed. ***I***, Representative contrast tuning

continued

curves of single cells. ***J***, Pattern contrast yielded half of the maximum response (C_{50}). Each box plot indicates a median marked by a solid line and a notch. The bottom and top edges of the boxes indicate 25th and 75th percentiles, and whiskers indicate maximum and minimum values in distributions. Crosses indicate individual values treated as outliers. Statistical analysis was performed using the Kruskal–Wallis test followed by Dunn–Sidak *post hoc* tests: $^{*}p < 0.05$, $^{**}p < 0.01$, $^{***}p < 0.001$.

Consequences of early rod degeneration to higher-order visual processing

The increased ERG b-wave sensitivity and remarkably well-preserved pattern-contrast sensitivity (Leinonen et al., 2020) point to adaptive functional re-arrangements in the *Rho*$^{P23H/WT}$ mouse retina during rod degeneration. But what happens at the V1 where the "conscious vision" is initially processed? To address this question, we recorded VEPs and single-cell responses in V1 to light ON/light OFF and drifting pattern stimuli in lightly anesthetized mice. First, as recent OMR data have already suggested (Leinonen et al., 2020), pattern contrast sensitivity remained excellent in *Rho*$^{P23H/WT}$ mice, and strikingly well-maintained even in the homozygous *Rho*$^{P23H/P23H}$ mice with extreme retinal degeneration (Fig. 6*I*). A corresponding persistent pattern-contrast sensitivity has been demonstrated by electrophysiology of the dorsal lateral geniculate (dLGN) nucleus in three- to five-week-old *Pde6β*^{Rd1} mice (Procyk et al., 2019). The *Pde6β*^{Rd1} mice at that age represent a late-stage retinal degeneration and have only a residual ERG response remaining (Strettoi et al., 2002). Similarly, the temporal-frequency threshold remained excellent in *Rho*$^{P23H/WT}$ mice, and was in fact elevated at one month of age (Fig. 6*G*,*H*). These data correspond well with the ERG (accelerated kinetics, Fig. 1; Extended Data Fig. 1-2; improved TCS by ERGs; Pasquale et al., 2021) and OMR findings in *Rho*$^{P23H/WT}$ mice (improved TCS by OMR; Pasquale et al., 2021). Nevertheless, we also found detrimental changes for V1 function starting already at one month of age in *Rho*$^{P23H/WT}$ mice (Figs. 5, 6). The light responses and spontaneous neuron firing were dramatically hyperexcited in the *Rho*$^{P23H/WT}$ mouse V1 (Figs. 4, 5). The observed hyperexcitability is well in line with previous literature, demonstrating increased neural noise originating from the inner retina (Borowska et al., 2011; Menzler and Zeck, 2011; Trenholm and Awatramani, 2015; Haselier et al., 2017; Telias et al., 2020). Further, as similarly indicated by the OMR behavior (Fig. 2), *Rho*$^{P23H/WT}$ mouse V1 neurons preferred lower SFs compared with WT mice (Fig. 6*E*), indicating increasing RGC receptive fields. However, the most striking abnormality we found was the severely debilitated orientation/direction tuning in *Rho*$^{P23H/WT}$ mice, which advanced to a practical absence of any direction preference by three months of age (Fig. 6*A*). It is challenging to speculate how these findings translate into clinical settings, because of the lack of corresponding data from RP patients. Hypersensitivity to bright light (called by the debated misnomer "photophobia") is common in RP (Hamel, 2006; Otsuka et al., 2020), and could in part result from similar hyperexcitation of the primary visual tract as observed in RP model mice. The relatively well-maintained behavioral vision of *Rho*$^{P23H/WT}$ mice may also be reflected in clinical settings, as many RP patients show minimal disturbances in subjective vision even at an advanced disease stage (Hartong et al., 2006).

Relevance to treatments in retinal degenerations

There are no pharmacotherapies available that would slow retinal degenerative diseases such as RP or dry age-related macular degeneration (Waugh et al., 2018). It is probable, however, that the impaired photoreception in these diseases can be augmented in the near future *via* novel therapies, such as photoreceptor transplantation (Pearson et al., 2012), chemical photoswitches (Tochitsky et al., 2018), optogenetic tools (Sahel et al., 2021), prosthetics (Lorach et al., 2015), stem cells (da Cruz et al., 2018; Foik et al., 2018), or gene therapy (Suh et al., 2020). But a great deal of concern has been raised whether, after blinding, the more complex inner retina is capable of normal signal processing and whether restored signals are adequate for sight. Second, most patients experience only a partial loss of vision and are not suitable for advanced vision restoration therapies; therefore, more conventional approaches are needed. Using the *Pde6β*^{Rd10} mouse model of RP, Telias et al. (2019) recently showed that the firing rate of RGCs spontaneously increased simultaneously with decreasing light responses after mouse eye-opening in multi-electrode array recordings. They were able to link the pathology with deteriorated visual behavior in a light avoidance test by decreasing spontaneous firing pharmacologically. Importantly, blocking the retinoic acid receptor decreased spontaneous RGC firing and increased visual behavior in *Pde6β*^{Rd10} mice (Telias et al., 2019, 2022). Another group used a different pharmacological strategy, a gap junction blockade, but showed similar beneficial effects, wherein a decrease in spontaneous firing of RGCs led to increased light responses (Toychiev et al., 2013). However, the speed of degeneration is faster and the mechanism of rod death is different in the *Pde6β*^{Rd10} mouse model as compared with the *Rho*$^{P23H/WT}$ mouse (Chang et al., 2007; Sakami et al., 2011), rendering direct comparisons difficult. It will be important in future experiments to test whether decreasing the noise signal of RGCs would be therapeutic also in other models of RP, including the *Rho*$^{P23H/WT}$ mouse with hyperexcited V1 (Figs. 3-6).

On the other hand, some recent studies have concluded positive/adaptive aspects of retinal reorganization after injury or during degeneration (Beier et al., 2017, 2018; Johnson et al., 2017; Care et al., 2019; Leinonen et al., 2020; Shen et al., 2020). For example,

Care and coworkers ablated 50% of rods in adult mice and uncovered functional compensation at the level of retinal interneurons, which recovered retinal output to near-normal levels (Care et al., 2020). Contextually similar conclusions of homeostatic adaptation to a partial retinal injury were drawn from rod/cone, cone, or rod bipolar cell ablation studies in adult rabbit, ground squirrel, and mouse retinas (Johnson et al., 2017; Beier et al., 2018; Care et al., 2019; Shen et al., 2020). We showed in the *Rho*$^{P23H/WT}$ mouse, representing a common form of human autosomal dominant RP, increased sensitivity to visual inputs at the photoreceptor-to-bipolar cell synapse and maintained rod-driven contrast sensitivity regardless of rod population loss of >50% (Leinonen et al., 2020). Importantly, functional adaptation to retinal stress has also been observed in glaucoma models, wherein increased excitability of RGCs and dLGN neurons may mitigate the loss of axon function caused by elevated intraocular pressure (Calkins, 2021; Van Hook et al., 2021).

Altogether, accumulating evidence suggests that retinal remodeling on photoreceptor degeneration may not solely possess disruptive elements, but may initially help the visual system by adapting to sensory function loss. As these countering elements seem to temporally overlap, it will be of utmost importance to uncover what are the original molecular triggers for the retinal rewiring and whether these signals divide into more than one downstream pathway. Will it be possible to pharmacologically intervene to promote neural adaptation while simultaneously suppressing the disruptive hyperexcitability? With respect to vision restoration trials in adult humans, neural plasticity will be crucial.

References

Albrecht DG, Hamilton DB (1982) Striate cortex of monkey and cat: contrast response function. J Neurophysiol 48:217–237.

Aleman TS, LaVail MM, Montemayor R, shuang Ying G, Maguire MM, Laties AM, Jacobson SG, Cideciyan AV (2001) Augmented rod bipolar cell function in partial receptor loss: an ERG study in P23H rhodopsin transgenic and aging normal rats. Vision Res 41:2779–2797.

Alitto HJ, Usrey WM (2004) Influence of contrast on orientation and temporal frequency tuning in ferret primary visual cortex. J Neurophysiol 91:2797–2808.

Beier C, Hovhannisyan A, Weiser S, Kung J, Lee S, Lee DY, Huie P, Dalal R, Palanker D, Sher A (2017) Deafferented adult rod bipolar cells create new synapses with photoreceptors to restore vision. J Neurosci 37:4635–4644.

Beier C, Palanker D, Sher A (2018) Stereotyped synaptic connectivity is restored during circuit repair in the adult mammalian retina. Curr Biol 28:1818–1824.e2.

Berson EL, Rosner B, Weigel-DiFranco C, Dryja TP, Sandberg MA (2002) Disease progression in patients with dominant retinitis pigmentosa and rhodopsin mutations. Invest Ophthalmol Vis Sci 43:3027–3036.

Borowska J, Trenholm S, Awatramani GB (2011) An intrinsic neural oscillator in the degenerating mouse retina. J Neurosci 31:5000–5012.

Brainard DH (1997) The psychophysics toolbox. Spat Vis 10:433–436.

Calkins DJ (2021) Adaptive responses to neurodegenerative stress in glaucoma. Prog Retin Eye Res 84:100953.

Camillo D, Ahmadlou M, Saiepour MH, Yasaminshirazi M, Levelt CN, Heimel JA (2018) Visual processing by calretinin expressing inhibitory neurons in mouse primary visual cortex. Sci Rep 8.

Carandini M, Ferster D (2000) Membrane potential and firing rate in cat primary visual cortex. J Neurosci 20:470–484.

Care RA, Kastner DB, De la Huerta I, Pan S, Khoche A, Della Santina L, Gamlin C, Santo Tomas C, Ngo J, Chen A, Kuo YM, Ou Y, Dunn FA (2019) Partial cone loss triggers synapse-specific remodeling and spatial receptive field rearrangements in a mature retinal circuit. Cell Rep 27:2171–2183.e5.

Care RA, Anastassov IA, Kastner DB, Kuo YM, Della Santina L, Dunn FA (2020) Mature retina compensates functionally for partial loss of rod photoreceptors. Cell Rep 31:107730.

Chang B, Hawes NL, Pardue MT, German AM, Hurd RE, Davisson MT, Nusinowitz S, Rengarajan K, Boyd AP, Sidney SS, Phillips MJ, Stewart RE, Chaudhury R, Nickerson JM, Heckenlively JR, Boatright JH (2007) Two mouse retinal degenerations caused by missense mutations in the beta-subunit of rod cGMP phosphodiesterase gene. Vision Res 47:624–633.

Choi EH, Suh S, Foik AT, Leinonen H, Newby GA, Gao XD, Banskota S, Hoang T, Du SW, Dong Z, Raguram A, Kohli S, Blackshaw S, Lyon DC, Liu DR, Palczewski K (2022) In vivo base editing rescues cone photoreceptors in a mouse model of early-onset inherited retinal degeneration. Nat Commun 13:1830.

da Cruz L, et al. (2018) Phase 1 clinical study of an embryonic stem cell–derived retinal pigment epithelium patch in age-related macular degeneration. Nat Biotechnol 36:328–337.

DeAngelis GC, Ohzawa I, Freeman RD (1993) Spatiotemporal organization of simple-cell receptive fields in the cat's striate cortex. II. Linearity of temporal and spatial summation. J Neurophysiol 69:1118–1135.

D'Orazi FD, Suzuki SC, Wong RO (2014) Neuronal remodeling in retinal circuit assembly, disassembly, and reassembly. Trends Neurosci 37:594–603.

Douglas RM, Alam NM, Silver BD, Mcgill TJ, Tschetter WW, Prusky GT (2005) Independent visual threshold measurements in the two eyes of freely moving rats and mice using a virtual-reality optokinetic system. Vis Neurosci 22:677–684.

Foik AT, Kublik E, Sergeeva EG, Tatlisumak T, Rossini PM, Sabe BA, Waleszczyk WJ, Sabel BA, Waleszczyk WJ, Sabe BA, Waleszczyk WJ (2015) Retinal origin of electrically evoked potentials in response to transcorneal alternating current stimulation in the rat. Invest Ophthalmol Vis Sci 56:1711–1718.

Foik AT, Lean GA, Scholl LR, McLelland BT, Mathur A, Aramant RB, Seiler MJ, Lyon DC (2018) Detailed visual cortical responses generated by retinal sheet transplants in rats with severe retinal degeneration. J Neurosci 38:10709–10724.

Foik AT, Scholl LR, Lean GA, Lyon DC (2020) Visual response characteristics in lateral and medial subdivisions of the rat pulvinar. Neuroscience 441:117–130.

Frankowski JC, Foik AT, Tierno A, Machhor JR, Lyon DC, Hunt RF (2021) Traumatic brain injury to primary visual cortex produces long-lasting circuit dysfunction. Commun Biol 4:1297.

Greenstein VC, Hood DC, Ritch R, Steinberger D, Carr RE (1989) S (blue) cone pathway vulnerability in retinitis pigmentosa, diabetes and glaucoma. Investig Ophthalmol Vis Sci 30:1732–1737.

Hamel C (2006) Retinitis pigmentosa. Orphanet J Rare Dis 1:40.

Hartong DT, Berson EL, Dryja TP (2006) Retinitis pigmentosa. Lancet 368:1795–1809.

Haselier C, Biswas S, Rösch S, Thumann G, Müller F, Walter P (2017) Correlations between specific patterns of spontaneous activity and stimulation efficiency in degenerated retina. PLoS One 12: e0190048.

Hassall MM, McClements ME, Barnard AR, Patricio M, Aslam SA, Maclaren RE (2020) Analysis of early cone dysfunction in an in vivo model of rod-cone dystrophy. Int J Mol Sci 21:1–18.

Jacobs GH, Neitz J, Deegan JF (1991) Retinal receptors in rodents maximally sensitive to ultraviolet light. Nature 353:655–656.

Johnson RE, Tien N-W, Shen N, Pearson JT, Soto F, Kerschensteiner D (2017) Homeostatic plasticity shapes the visual system's first synapse. Nat Commun 8:1220.

Jones BW, Pfeiffer RL, Ferrell WD, Watt CB, Marmor M, Marc RE (2016) Retinal remodeling in human retinitis pigmentosa. Exp Eye Res 150:149–165.

Kleiner M, Brainard D, Pelli D, Ingling A, Murray R, Broussard C (2007) What's new in psychtoolbox-3. Perception 36:1–16.

Kordecka K, Foik AT, Wierzbicka A, Waleszczyk WJ (2020) Cortical inactivation does not block response enhancement in the superior colliculus. Front Syst Neurosci 14:1–11.

Kretschmer F, Kretschmer V, Kunze VP, Kretzberg J (2013) OMR-arena: automated measurement and stimulation system to determine mouse visual thresholds based on optomotor responses. PLoS One 8:e78058.

Kretschmer F, Sajgo S, Kretschmer V, Badea TC (2015) A system to measure the optokinetic and optomotor response in mice. J Neurosci Methods 256:91–105.

Leinonen H, Keksa-Goldsteine V, Ragauskas S, Kohlmann P, Singh Y, Savchenko E, Puranen J, Malm T, Kalesnykas G, Koistinaho J, Tanila H, Kanninen KM (2017) Retinal degeneration in a mouse model of CLN5 disease is associated with compromised autophagy. Sci Rep 7.

Leinonen H, Pham NC, Boyd T, Santoso J, Palczewski K, Vinberg F (2020) Homeostatic plasticity in the retina is associated with maintenance of night vision during retinal degenerative disease. Elife 9: e59422.

Lewandowski D, et al. (2022) Inhibition of ceramide accumulation in AdipoR1-/- mice increases photoreceptor survival and improves vision. JCI Insight 7.

Lorach H, Goetz G, Smith R, Lei X, Mandel Y, Kamins T, Mathieson K, Huie P, Harris J, Sher A, Palanker D (2015) Photovoltaic restoration of sight with high visual acuity. Nat Med 21:476–482.

Lyubarsky AL, Falsini B, Pennesi ME, Valentini P, Pugh EN (1999) UV- and midwave-sensitive cone-driven retinal responses of the mouse: a possible phenotype for coexpression of cone photopigments. J Neurosci 19:442–455.

Machida S, Kondo M, Jamison JA, Khan NW, Kononen LT, Sugawara T, Bush RA, Sieving PA (2000) P23H rhodopsin transgenic rat: correlation of retinal function with histopathology. Invest Ophthalmol Vis Sci 41:3200–3209.

Marc R, Pfeiffer R, Jones B (2014) Retinal prosthetics, optogenetics, and chemical photoswitches. ACS Chem Neurosci 5:895–901.

Menzler J, Zeck G (2011) Network oscillations in rod-degenerated mouse retinas. J Neurosci 31:2280–2291.

Naka KI, Rushton WA (1966) S-potentials from luminosity units in the retina of fish (Cyprinidae). J Physiol 185:587–599.

Orban T, Leinonen H, Getter T, Dong Z, Sun W, Gao S, Veenstra A, Heidari-Torkabadi H, Kern TS, Kiser PD, Palczewski K (2018) A combination of G protein-coupled receptor modulators protects photoreceptors from degeneration. J Pharmacol Exp Ther 364:207–220.

Otsuka Y, Oishi A, Miyata M, Oishi M, Hasegawa T, Numa S, Ikeda HO, Tsujikawa A (2020) Wavelength of light and photophobia in inherited retinal dystrophy. Sci Rep 10:14798.

Pasquale RL, Guo Y, Umino Y, Knox B, Solessio E (2021) Temporal contrast sensitivity increases despite photoreceptor degeneration in a mouse model of retinitis pigmentosa. eNeuro 8:ENEURO.0020-21.2021.

Pearson RA, Barber AC, Rizzi M, Hippert C, Xue T, West EL, Duran Y, Smith AJ, Chuang JZ, Azam SA, Luhmann UFO, Benucci A, Sung CH, Bainbridge JW, Carandini M, Yau K-W, Sowden JC, Ali RR (2012) Restoration of vision after transplantation of photoreceptors. Nature 485:99–103.

Pelli DG (1997) The VideoToolbox software for visual psychophysics: transforming numbers into movies. Spat Vis 10:437–442.

Pfeiffer RL, Marc RE, Jones BW (2020) Persistent remodeling and neurodegeneration in late-stage retinal degeneration. Prog Retin Eye Res 74:100771.

Procyk CA, Allen AE, Martial FP, Lucas RJ (2019) Visual responses in the dorsal lateral geniculate nucleus at early stages of retinal degeneration in rd1 PDE6β mice. J Neurophysiol 122:1753–1764.

Przybyszewski AW, Kagan I, Snodderly DM (2014) Primate area V1: largest response gain for receptive fields in the straight-ahead direction. Neuroreport 25:1109–1115.

Reh TA (2016) Photoreceptor transplantation in late stage retinal degeneration. Invest Ophthalmol Vis Sci 57:ORSFg1–ORSFg7.

Ronning KE, Allina GP, Miller EB, Zawadzki RJ, Pugh EN Jr, Hermann R, Burns ME (2018) Loss of cone function without degeneration in a novel Gnat2 knock-out mouse. Exp Eye Res 171:111–118.

Sahel JA, Boulanger-Scemama E, Pagot C, Arleo A, Galluppi F, Martel JN, Esposti SD, Delaux A, de Saint Aubert J-B, de Montleau C, Gutman E, Audo I, Duebel J, Picaud S, Dalkara D, Blouin L, Taiel M, Roska B (2021) Partial recovery of visual function in a blind patient after optogenetic therapy. Nat Med 27:1223–1229.

Sakami S, Maeda T, Bereta G, Okano K, Golczak M, Sumaroka A, Roman AJ, Cideciyan AV, Jacobson SG, Palczewski K (2011) Probing mechanisms of photoreceptor degeneration in a new mouse model of the common form of autosomal dominant retinitis pigmentosa due to P23H opsin mutations. J Biol Chem 286:10551–10567.

Sakami S, Kolesnikov AV, Kefalov VJ, Palczewski K (2014) P23H opsin knock-in mice reveal a novel step in retinal rod disc morphogenesis. Hum Mol Genet 23:1723–1741.

Schwarz C, Sharma R, Cheong SK, Keller M, Williams DR, Hunter JJ (2018) Selective S cone damage and retinal remodeling following intense ultrashort pulse laser exposures in the near-infrared. Invest Ophthalmol Vis Sci 59 59:5973–5984.

Shen N, Wang B, Soto F, Kerschensteiner D (2020) Homeostatic plasticity shapes the retinal response to photoreceptor degeneration. Curr Biol 30:1916–1926.e3.

Soto F, Kerschensteiner D (2015) Synaptic remodeling of neuronal circuits in early retinal degeneration. Front Cell Neurosci 9:395.

Strettoi E (2015) A survey of retinal remodeling. Front Cell Neurosci 9:494.

Strettoi E, Porciatti V, Falsini B, Pignatelli V, Rossi C (2002) Morphological and functional abnormalities in the inner retina of the rd/rd mouse. J Neurosci 22:5492–5504.

Strettoi E, Marco D, Orsini B, Napoli N, Retinal D, Strettoi E, Marco B Di, Orsini N, Napoli D (2022) Retinal plasticity. Int J Mol Sci 23:1138.

Suh S, Choi EH, Leinonen H, Foik AT, Newby GA, Yeh WH, Dong Z, Kiser PD, Lyon DC, Liu DR, Palczewski K (2020) Publisher correction: restoration of visual function in adult mice with an inherited retinal disease via adenine base editing. Nat Biomed Eng 4:1119.

Telias M, Denlinger B, Helft Z, Thornton C, Beckwith-Cohen B, Kramer RH (2019) Retinoic acid induces hyperactivity, and blocking its receptor unmasks light responses and augments vision in retinal degeneration. Neuron 102:574–586.e5.

Telias M, Nawy S, Kramer RH (2020) Degeneration-dependent retinal remodeling: looking for the molecular trigger. Front Neurosci 14:618019.

Telias M, Sit KK, Frozenfar D, Smith B, Misra A, Goard MJ, Kramer RH (2022) Retinoic acid inhibitors mitigate vision loss in a mouse model of retinal degeneration. Sci Adv 8:eabm4643.

Tochitsky I, Kienzler MA, Isacoff E, Kramer RH (2018) Restoring vision to the blind with chemical photoswitches. Chem Rev 118:10748–10773.

Toychiev AH, Ivanova E, Yee CW, Sagdullaev BT (2013) Block of gap junctions eliminates aberrant activity and restores light responses during retinal degeneration. J Neurosci 33:13972–13977.

Trenholm S, Awatramani GB (2015) Origins of spontaneous activity in the degenerating retina. Front Cell Neurosci 9:277.

Van Den Bergh G, Zhang B, Arckens L, Chino YM (2010) Receptive-field properties of V1 and V2 neurons in mice and macaque monkeys. J Comp Neurol 518:2051–2070.

Van Hook MJ, Monaco C, Bierlein ER, Smith JC (2021) Neuronal and synaptic plasticity in the visual thalamus in mouse models of glaucoma. Front Cell Neurosci 14:476.

Waugh N, Loveman E, Colquitt J, Royle P, Yeong JL, Hoad G, Lois N (2018) Treatments for dry age-related macular degeneration and Stargardt disease: a systematic review. Health Technol Assess 22:1–168.

Xu M, Zhai Y, MacDonald IM (2020) Visual field progression in retinitis pigmentosa. Invest Ophthalmol Vis Sci 61:56.